Journal of Materials Chemistry C

# Combinatorial investigation of structural and optical properties of cation-disordered $ZnGeN_2$

| | |
|---|---|
| Journal: | *Journal of Materials Chemistry C* |
| Manuscript ID | TC-ART-04-2020-001675.R1 |
| Article Type: | Paper |
| Date Submitted by the Author: | 21-May-2020 |
| Complete List of Authors: | Melamed, Celeste; National Renewable Energy Laboratory, ; Colorado School of Mines, Physics<br>Pan, Jie; National Renewable Energy Laboratory, Chemical and Materials Cdnter<br>Mis, Allison; Colorado School of Mines, Department of Metallurgical and Materials Engineering; National Renewable Energy Laboratory<br>Heinselman, Karen; National Renewable Energy Laboratory<br>Schnepf, Rekha; Colorado School of Mines, Physics<br>Woods-Robinson, Rachel; University of California Berkeley, Applied Science and Technology; E O Lawrence Berkeley National Laboratory,<br>Cordell, Jacob; National Renewable Energy Laboratory; Colorado School of Mines, Mechanical Engineering<br>Lany, Stephan; National Renewable Energy Laboratory,<br>Toberer, Eric; Colorado School of Mines,<br>Tamboli, Adele; National Renewable Energy Lab, ; Colorado School of Mines, Physics |
| | |

Journal Name

ARTICLE TYPE

Cite this: DOI: 00.0000/xxxxxxxxxx

# Combinatorial investigation of structural and optical properties of cation-disordered $ZnGeN_2$

Celeste L. Melamed,[a,b] Jie Pan,[a] Allison Mis,[a,c] Karen Heinselman,[a] Rekha R. Schnepf,[a,b] Rachel Woods-Robinson,[a,d] Jacob J. Cordell,[a,e] Stephan Lany,[a] Eric S. Toberer,[b,a] and Adele C. Tamboli*[a,b]

Received Date
Accepted Date

DOI: 00.0000/xxxxxxxxxx

Cation-disordered $ZnGeN_2$ shows promise for application as a blue-green emitter in light-emitting devices, but more foundational work is necessary to understand structure-property relationships. In this work, we present a combinatorial exploration of the experimental phase space of wurtzite (cation-disordered) $ZnGeN_2$ using high-throughput co-sputtering. Structure, morphology and optical properties are explored as a function of cation composition and synthesis temperature. $ZnGeN_2$ is found to crystallize in the wurtzite structure ranging from Zn-rich to Ge-rich compositions. X-ray diffraction refinements reveal a continuous shift in cell volume with off-stoichiometry, indicating alloy-like structural behavior. The optical absorption of all films examined is lower in energy than the value predicted for cation-ordered $ZnGeN_2$, suggesting that cation disorder is decreasing the bandgap. Additionally, the absorption threshold shifts continuously to higher energy for Ge-rich samples, consistent with bandgap shifts due to alloy-like structural behavior. Defect formation energy diagrams are calculated to help guide understanding of off-stoichiometry from a defect complex perspective. This work paves the way toward use of $ZnGeN_2$ as a bandgap-tunable optoelectronic semiconductor.

## 1 Introduction

The III-V family of semiconductor compounds has revolutionized optoelectronics, such as the InN-GaN alloy system, which enabled the 2014 Nobel Prize for highly efficient blue LEDs.[1,2] However, outstanding challenges remain in the field of solid-state lighting. The development of efficient color-mixed LEDs could increase efficiency by >30% from the current lossy phosphor-converted LEDs.[3] However, the lack of efficient emitters in the 500-600 nm range (termed the "green gap") has been a known challenge in the field for decades.[4] The InGaN alloy system is typically used as a green emitter, but these materials are inefficient due to the miscibility gap between InN and GaN.[5] Indeed, there is a general lack of optoelectronic materials with band gap energies in the $2-3$ eV range, especially that can be integrated with III-V's and silicon. Looking to new compounds may bring new and energy-efficient solutions to this long-standing problem.

An alternative option to the III-Vs is to explore structurally analogous materials created by cation mutation (also known as structural analogy), in which an element in a structure is replaced with two elements averaging to the same valence. This strategy has been employed since the mid-1900s in order to discover a number of groundbreaking optoelectronic materials.[6,7] Replacement of the Group III elements in the III-V family yields the II-IV-$V_2$ family of semiconductors; for example, $ZnGeN_2$ is analogous to GaN.[8] This family has many constituents and is understudied for optoelectronic applications, offering a rich field to explore. Additionally, the II-IV-$V_2$ compounds typically crystallize in either a cation-ordered or disordered structure, which has been shown to impact the bandgap.[9] $ZnGeN_2$ is a promising II-IV-$V_2$ material for LED applications, with a bandgap of ~3.5 eV and lattice-matching enabling integration with existing GaN technology.[10,11] Within this class of materials, calculations have suggested that cation site disorder lowers the bandgap by as much as 1 eV with little corresponding change in lattice parameters.[12,13] If similar behavior occurs for $ZnGeN_2$, a bandgap energy in the green (~2.5 eV) would be obtained. However, significant questions remain regarding the fundamentals of $ZnGeN_2$ before it can

[a] National Energy Laboratory, Golden, CO, USA. Fax:+1-303-384-7600; Tel:+1-303-384-7223; E-mail: adele.tamboli@nrel.gov
[b] Department of Physics, Colorado School of Mines, Golden, CO, USA.
[c] Department of Metallurgical and Materials Engineering, Colorado School of Mines, Golden, CO, USA.
[d] Department of Physics, University of California Berkeley, Berkeley, CA, USA.
[e] Department of Mechanical Engineering, Colorado School of Mines, Golden, CO, USA.

† Electronic Supplementary Information (ESI) available: Rutherford backscattering spectroscopy scans of two representative $ZnGeN_2$ samples; additional scanning electron microscopy images; optical constants (refractive index and extinction coefficient) for representative samples; an example input file used to run Pawley refinements of X-ray diffraction data. See DOI: 00.0000/00000000.

be used as an emitter. In this work, we explore the structural and optical properties of $ZnGeN_2$ as a function of synthesis temperature and cation off-stoichiometry. Deconvolving these fundamental properties will pave the way for the use of $ZnGeN_2$ as a green emitter, enabling high-efficiency color-mixed LEDs and solving the decades-long "green gap" problem.

While $ZnGeN_2$ has been synthesized since the 1970s, many significant questions remain regarding its structure and properties.[14] In $ZnGeN_2$, the cation ordered and disordered structures can be distinguished using X-ray diffraction; the ordered (orthorhombic) ground state exhibits peak splitting which is detectable on a laboratory diffractometer.[15] Control of cation site ordering has been demonstrated using synthesis temperature and post-growth annealing for bulk samples, but has yet to be correlated with optical properties.[15] Crystalline and epitaxial thin films have been synthesized with sputtering, molecular beam epitaxy (MBE), and metal-organic chemical vapor deposition (MOCVD), but no thorough connection between cation site disorder and optoelectronic properties has been established.[16–20] Reported bandgaps range from 2.7 to 3.4 eV, but with no clear determining trend.[19–26] Furthermore, the optical properties of high-quality disordered material have not yet been fully explored. Though it has been computationally predicted in the similar system $ZnSnN_2$ that cation disorder will continuously shift the band edges and cause a band-tail-like appearance in absorption (versus the introduction of deep defects),[27] the bandgap tuning mechanism has not been experimentally established; this question is discussed further in a review by Schnepf et. al.[28] Since $ZnGeN_2$ has historically been treated like a line compound, there are likely unreported compositional variations that have not been characterized, which could contribute to the inconsistencies in the literature. While we refer to $ZnGeN_2$ as a compound with presumed integer stoichiometry throughout this work, we discuss cation composition $x$ with a corresponding film stoichiometry of $Zn_{2x}Ge_{2-2x}N_2$; the $x$ is omitted for simplicity. Additionally, the literature on powder $(Zn_{1+x}Ge)(N_2O_x)$ and the recent report by Breternitz *et al.* in Ref. 29 suggests that dilute oxygen content results in a wurtzite $ZnGeN_2$-ZnO alloy structure, likely due to Zn atoms preferentially bonding with O and trapping cation disorder in the system.[30–34] Our recent report in Ref. 35 of a cation-disordered $ZnGeN_{2-x}O_x$ epitaxial film with ∼9% O/(O+N) confirms this oxynitride behavior in thin film form. Thus, to draw conclusions about the intrinsic properties of $ZnGeN_2$, it is crucial to synthesize material with minimal oxygen contamination and to carefully characterize composition.

The analogous compound $ZnSnN_2$, which has experienced a surge of recent interest for PV applications,[36] offers some guidance into the important questions to investigate for $ZnGeN_2$. It has been found that $ZnSnN_2$ does not just act like a line compound, but exhibits a large tolerance to cation off-stoichiometry.[37] In fact, the lowest reported carrier density material was synthesized at ∼67% Zn/(Zn+Sn), suggesting that cation off-stoichiometry can be used as a parameter to tune optoelectronic properties.[38] An additional lesson from the $ZnSnN_2$ literature is the importance of unintentional oxygen incorporation. Fioretti *et al.* in Ref. 39 found that films containing 14 at.% oxygen were exhibiting lattice parameter shifts consistent with an alloy model between $ZnSnN_2$ and ZnO. They hypothesized that at Zn-rich compositions, excess Zn and unintentional O is forming charge-neutral defect complexes which reduce the degenerate carrier density of the compound. This research again suggests that characterization of both anion and cation stoichiometry is key to understanding structure-property relationships in $ZnGeN_2$.

To begin deconvolving the historically intertwined impacts of oxygen, stoichiometry and structure on the Zn-Ge-N system, cation-disordered $ZnGeN_2$ films with varying cation compositions and minimal oxygen were prepared. Combinatorial thin film growth enabled a large experimental phase space to be rapidly accessed. Cation composition was characterized with X-ray fluorescence and anion composition was examined with Rutherford backscattering spectroscopy in order to insure minimal oxygen incorporation. To understand ordering on the cation site, films were characterized with both in-house and synchrotron X-ray diffraction. In order to characterize trends in optical properties as a function of composition and structure, spectroscopic ellipsometry was modelled. Finally, experimental results are understood through the lens of first principles calculations on native defects.

## 2 Experimental Methods

$ZnGeN_2$ was deposited by radio frequency co-sputtering onto stationary 2"×2" substrates. Metallic zinc and germanium targets were angled at 45° to the substrate normal to create a gradient in cation flux during synthesis. This geometry generates a continuous gradient in composition on each substrate, resulting in a thin film sample with varying synthesis conditions henceforth called a "sample library." The power ratio between the two sputtering cathodes was used to control the stoichiometry range of each sample library. Experimental modifications (such as a thorough chamber baking routine and a load lock) enabled a base vacuum pressure in the range $2\times10^{-8}$–$6\times10^{-9}$ Torr, a 2 order-of-magnitude decrease from prior literature from our group.[35] This resulted in much less ambient oxygen and water present in the vacuum system, decreasing the oxygen contamination in sputtered films and allowing conclusions to be drawn about the intrinsic properties of the Zn-Ge-N system. This chamber was maintained at a working pressure of 12 mTorr during deposition with a gas flow of 15 sccm $N_2$ and 5 sccm Ar. This chamber utilized 3" diameter sputtering cathodes, which were operated over a range of powers from 20 W to 210 W at a distance of ∼12 in from the substrate. Cathodes were sputtered with closed shutters for 40-60 minutes before deposition in order to clean the target surfaces. All nitrogen gas was flowed through an electron cyclotron resonance (ECR) plasma source pointed orthogonally to the substrate in order to supply reactive nitrogen during growth. The ECR source was operated at 150 W with a bias current of 19.5 A. Samples were grown on single crystal silicon wafers with either native oxide or 100 nm thermal oxide in order to facilitate electrical measurements.

Films were first characterized using the suite of spatially resolved characterization tools available at the National Renewable Energy Laboratory, which has been used for previous Zn-IV-$N_2$ work.[37,39,40] These tools collect measurements at the same stan-

dardized positions on each sample library, enabling straightforward correlation between properties. A standard characterization grid of 4×11 points was used for all samples. All mapping data was then loaded and processed using COMBIgor, a custom combinatorial data analysis package built in Igor Pro.[41] This software enables easy handling of the large amounts of data generated by combinatorial experiments, as well as rapid data processing such as background subtraction and normalization.

Cation composition, here reported as %Zn/(Zn+Ge), was characterized using X-ray fluorescence (XRF) with Rh L-series excitation in energy-dispersive mode using Fischer XDV-SDD software. X-ray diffraction (XRD) was performed using a Bruker D8 Discover equipped with an area detector. Unit cell parameters were extracted using Pawley refinement of X-ray diffraction data using the TOPAS 6 Academic software package. The hexagonal wurtzite structure was used as the base structure for refinement. An example input file is shown in the Supplementary Information (Fig. S4). Optical characterization was performed with a J.A. Woollam Co. M-2000 variable angle spectroscopic ellipsometer. To maximize measurement sensitivity, data was collected at three angles around the Brewster angle of Si. The resulting data was analyzed using CompleteEase software by modeling the sputtered films with a Kramers-Kronig consistent B-Spline parameterization, which allows for extraction of the film dielectric function without any assumptions about the films.[42] Roughness and thickness non-uniformity were included in the models to account for non-idealities due to combinatorial sputter synthesis. Models were then used to generate optical constants and absorption coefficient values as a function of energy; only models with a mean squared error (MSE) of less than 25 were included in data analysis.

A representative selection of sample libraries were taken to the Stanford Synchrotron Radiation Lightsource (SSRL) at the SLAC National Laboratory for structural analysis. Mapping was performed with Wide Angle X-ray Scattering (WAXS) on Beam Line 1-5. 2D scattering was collected with a Rayonix 165 CCD Camera at grazing incidence at an incident energy of 12.7 keV, and peaks were integrated between 5° and 175° $\chi$.

To investigate anion composition, Rutherford backscattering spectroscopy (RBS) was performed in a 168° backscattering geometry with a 2 MeV He+ beam energy using a model 3S-MR10 RBS system from National Electrostatics Corporation. A 2 MeV beam energy was used to avoid the non-Rutherford resonant scattering that occurs at 3 MeV for nitrogen and oxygen. Samples were measured until the total integrated charge delivered to the sample was 160 $\mu$C and 200 $\mu$C respectively. The film composition was determined by fitting using the RUMP analysis software[43] with the major cation ratio fixed at Zn/(Zn+Ge) ratios determined by XRF since Zn and Ge are too close in mass to be distinguished by RBS using this beam energy.

Film morphology was examined with scanning electron microscopy (SEM) and transmission electron microscopy (TEM). TEM micrographs were acquired with an FEI Co. Talos F200X transmission electron microscope with scanning capabilities operating at an accelerating voltage of 200 keV. Specimens for TEM were prepared from sputtered films via in-situ focused ion beam lift-out methods[44] using an FEI Co. Helios Nanolab 600i SEM/FIB DualBeam workstation. Specimens were ion milled at 2 keV and 77 pA to remove Ga ion beam damage and achieve a final thickness of approximately 100 nm. STEM bright field (BF) and high-angle annular dark field (HAADF) images were acquired at a camera length of 77 mm. Chemical mapping was performed in the TEM using the Super-X energy-dispersive X-ray spectroscopy (EDS) system.

First-principles defect calculations were carried out using the Vienna Ab initio Simulation Package (VASP) implementing projector-augmented-wave (PAW) potentials.[45] The Generalized Gradient Approximation (GGA)[46] was used to account for the electron exchange-correlation energies. On site Coulomb interactions (DFT+$U$) for Zn-d orbitals ($U$=6 eV) were used following the Dudarev approach.[47] Soft pseudopotentials were used for N and O with a cut-off energy of 380 eV for the plane wave basis set. The ordered ground state of $ZnGeN_2$ used for defect supercells has an orthorhombic crystal structure in the space group $Pna2_1$ (space group 33). A $2\times2\times2$ supercell of the ground state structure containing 128 atoms was used for defect calculations; these supercells were relaxed using $2\times2\times2$ Gamma-centered $k$-point mesh. In defect calculations, electronic step convergence was set to less than $10^{-5}$ eV per supercell while force convergence was set below 0.02 eV on each atom. The electronic band gap is corrected by GW calculations as implemented in Ref. 48.

The calculated band gap of 3.63 eV for the $ZnGeN_2$ ordered ground state structure (space group 33) and the corresponding absorption spectrum were obtained from GW calculations in the NREL Materials Database (please see Refs. 49,50 for computational details).

## 3 Results

### 3.1 Composition

The experimental phase space explored in this work is shown in Fig. 1. Synthesis temperatures ranging from ambient to 600°C were explored, with resulting cation compositions ranging from 80% Zn at low temperatures to nearly 0% at high temperatures as characterized by XRF and confirmed by EDS. Each unique color in Fig. 1 represents a different sample library synthesized, and consequently a large region of phase space was explored with only ∼10 depositions. This experimental phase map also demonstrates that the the entire temperature-composition space of $ZnGeN_2$ is not easily accessible by sputtering; mainly, Zn incorporation becomes difficult at high temperatures even when the Zn:Ge cathode power ratio is increased drastically. At deposition temperatures of 500°C, even a Zn:Ge cathode power ratio of 10:1 was found to result in Ge-rich films. Zn loss at high temperatures is likely due to the vapor pressure of Zn, which is already 0.1 torr at 400°C. Consequently, this work focuses on synthesis experiments performed at and below 500°C.

In order to deconvolve the effects of oxygen contamination on the properties of $ZnGeN_2$, careful characterization with Rutherford backscattering spectroscopy (RBS) was performed to ensure minimal contamination. RBS reveals oxygen incorporation of <5% O/(O+N), which is approaching the detection limit of the

scans performed. RBS scans for two representative Ge-rich samples grown at 400°C and 500°C are included in the Supplementary Information (Fig. S1). Models are shown with and without oxygen to demonstrate how the oxygen level is approaching the noise in the data. Thus, in this study the impact of oxygen content will be assumed to be negligible, allowing conclusions to be drawn about intrinsic properties of $ZnGeN_2$ without alloying on the anion site.

### 3.2 Structure

Both in-house and synchrotron X-ray diffraction with a 2D detector were performed on the sample libraries shown in Fig. 1, and the phase space where crystallinity is observed is shaded in purple. All samples outside of the shaded region (including those grown at ambient temperatures) were amorphous. All crystalline films exhibited the wurtzite structure characteristic of cation-disordered $ZnGeN_2$, even up to synthesis temperatures of 600°C. This is expected due to the structural reports of $ZnGeN_2$ in the literature; all reports of orthorhombic (cation-ordered) $ZnGeN_2$ were synthesized or annealed at 800°C or above, which this study is well below due to the challenges associated with the vapor pressure of Zn.[15] Despite the fact that cation-ordered $ZnGeN_2$ is the ground state structure, it is likely that the rapid growth rate and lower temperatures of sputtering does not allow enough adatom mobility for these films to achieve ordering.[28]

Selected examples of synchrotron XRD as a function of cation composition and synthesis temperature are shown in Fig. 2. No secondary phases are observed, and the peak triplet which is characteristic of wurtzite can be clearly seen between 2.0 and 3.0 $Å^{-1}$. Peak splitting of the first and third peaks of this triplet, which would indicate the cation-ordered (orthorhombic) superstructure, is not detected in any of these libraries. At 40 and 45% Zn/(Zn+Ge), as shown in Fig. 2a-b, films exhibit in-plane texturing, with the (100) and (101) reflections showing the strongest intensities. At 50% Zn/(Zn+Ge), the (002) peak begins to appear at all temperatures. For the highest Zn concentration, 55%, films become strongly (002) textured. This is consistent with previously reported depositions in a high base-pressure background, which shift from polycrystalline to epitaxial with increasing Zn content due to improved surface adatom mobility (as shown in Ref 35).

Pawley refinements were performed in order to extract lattice parameters and cell volume. Wurtzite lattice parameters and cell volume are shown in Fig. 3 as a function of cation composition, with black diamonds indicating values reported in the literature. Our reported values are consistent with the literature values, especially when considering that these reports do not precisely characterize cation composition (literature values are placed at 50% Zn/(Zn+Ge) for simplicity).[10,17,20] At Ge-rich cation compositions ex. 40% Zn/(Zn+Ge), the in-plane lattice parameter *a* contracts to smaller values as a function of synthesis temperature. Not all samples were able to be fit for *c* lattice parameter due to

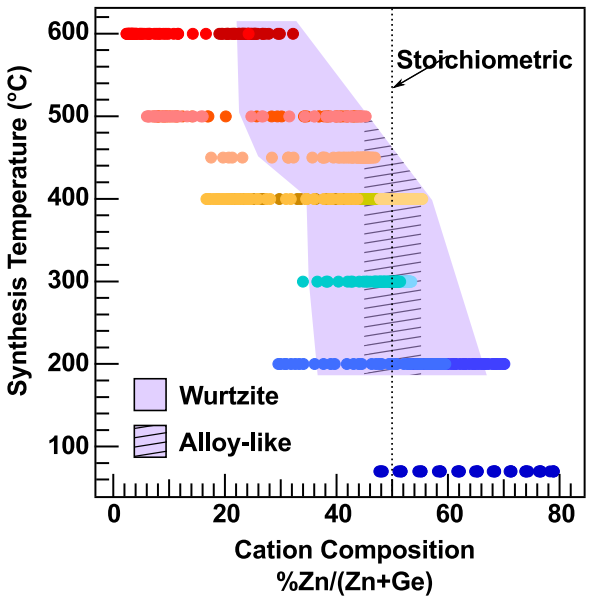


Fig. 1 Combinatorial sputtering of $ZnGeN_2$ was performed over a wide range of synthesis temperatures and metallic gun power ratios, yielding a large experimental phase map accessible by sputtering. Each unique color shown on this plot is a different sample library. The area shaded in purple is the region found to exhibit wurtzite crystallinity by XRD, and the hatched region exhibits alloy-like shifts in cell volume (discussed in the Structure section). All samples outside of the shaded region were found to be amorphous.

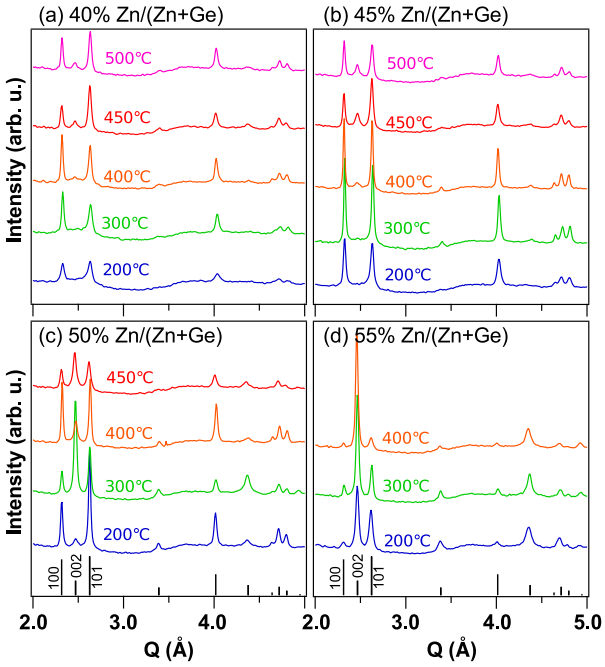


Fig. 2 Synchrotron diffraction as a function of cation composition and temperature. (a-b) At cation compositions of 40 and 45% Zn/(Zn+Ge), films exhibit some in-plane texturing, with the (100) and (101) reflections exhibiting the strongest intensities. (c) At 50% Zn/(Zn+Ge), the diffraction spectra appear more polycrystalline in nature, with all peaks appearing at all temperatures. (d) When films are grown in a Zn-rich regime of 55% Zn/(Zn+Ge), texturing becomes much stronger in the (002) orientation. In general, no clear trends are observed with synthesis temperature. The wurtzite $ZnGeN_2$ reference trace is shown in black (slightly shifted in Q to take into account peak shifting and a misalignment of the sample stage).

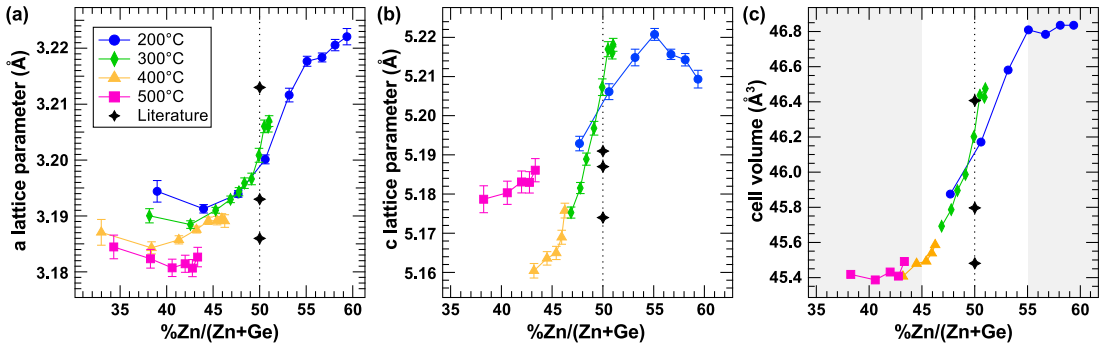


Fig. 3 Pawley refinements were performed to extract wurtzite lattice parameters (a-b). Ideal stoichiometry (50%) is indicated by a black dashed line. Literature data for wurtzite $ZnGeN_2$ (black stars) is shown at 50% for simplicity even when the exact composition was not determined.[10,17,20]. The calculated cell volume is shown in (c); the gray shaded regions indicate where cell volume has plateaued and is no longer behaving in an alloy-like manner.

preferential orientation, so no further trends with synthesis temperature can be elucidated from this data. In Fig. 3c, the cell volume exhibits a continuous shift to larger values with increasing Zn cation composition. Between 45 and 55% Zn/(Zn+Ge), this shift in cell volume is linear, while it plateaus outside of these compositions (shaded in gray). Within the regime of linear volume change, the shift is consistent with increasing $Zn_{Ge}$ and $Ge_{Zn}$ antisites for Zn and Ge rich conditions respectively due to the slightly larger atomic radius of Zn. Thus, the cation off-stoichiometry within the $45-55$% range (hatched in Fig. 1) is being incorporated into the $ZnGeN_2$ lattice in an alloy-like manner, despite $ZnGeN_2$ nominally being a line compound. It is important to note that though the binary metal nitrides of Zn and Ge exhibit stable structures ($Zn_3N_2$ and $Ge_3N_4$), they are not wurtzite.[51,52] Thus, the alloy-like behavior exhibited in $ZnGeN_2$ is not a traditional alloy between two binary compounds. This behavior is enabled by the similar atomic sizes of Zn and Ge and by the presence of disorder on the cation site. Outside of the $45-55$% composition range, the cell volume plateaus, indicating another mechanism such as amorphous incorporation or segregation at grain boundaries is enabling further off-stoichiometry.

### 3.3 Morphology

Scanning electron microscopy (SEM) was performed on a selection of points on sample libraries grown with varying conditions. Fig. 4 shows a series of samples at a constant composition of 45% Zn/(Zn+Ge) synthesized at (a) 200°C, (b) 400°C, (c) 450°C and (d) 500°C. The grain sizes observed here of $10-50$ nm are consistent with previous films grown by combinatorial sputtering.[37] Cross-sectional SEM is shown in the Supplementary Information (Fig. S2), and reveals dense and columnar grain growth as expected for sputtered combinatorial thin films.[37] At a synthesis temperature of 200°C (Fig. 4a), the film exhibits very small surface features with smooth and non-oriented grains. With increasing synthesis temperature, larger and sharper grains begin to appear. These features appear triangular pyramidal in shape and are most clearly observed at 500°C. Similar surface faceting is shown in a Zn-rich sample library as well (shown in Fig. S2 of the Supplementary Information). Faceting such as this typically indicates that growth conditions are non-diffusion limited and are thus closer to equilibrium;[53] faceting has been observed in molecular beam epitaxy (MBE) grown $ZnGeN_2$ thin films previously.[25] This faceting does not appear on any samples with stoichiometric compositions (Fig. S2), which may indicate that synthesizing $ZnGeN_2$ off-stoichiometry improves adatom mobility. Faceting also tends to occur coincident with strong crystallographic texturing as characterized by XRD. Additionally, the fact that faceting occurs in these cation disordered samples indicates that site disorder can coexist with non-kinetically-limited growth.

Fig. 5 shows TEM HAADF, BF, and EDS maps for a sample synthesized at 300°C with cation composition of 45% Zn/(Zn+Ge) (thus, within the alloy-like region). This data is consistent with cross-sectional SEM (Fig. S2): dense, columnar grains are observed, similar to those observed previously in the literature on

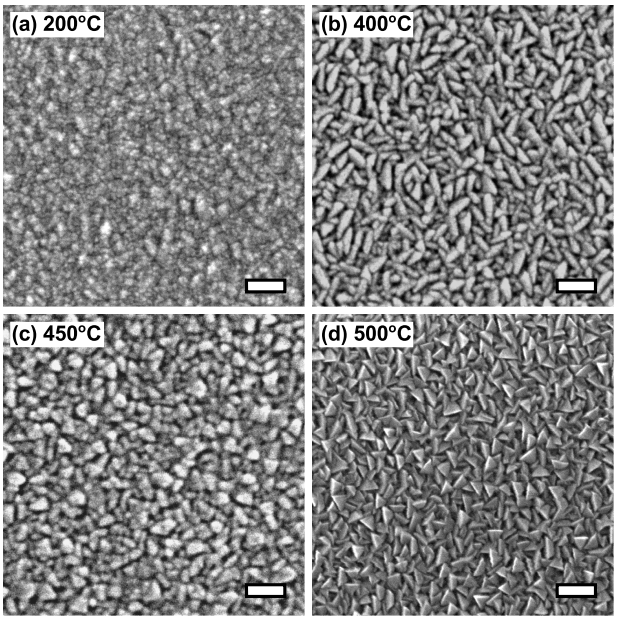


Fig. 4 Scanning electron microscopy images of a set of samples with cation compositions of 45% Zn/(Zn+Ge), shown as a function of synthesis temperature. Samples shown were grown at temperatures of (a) 200°C, (b) 400°C, (c) 450°C and (d) 500°C. All scale bars are 100 nm.

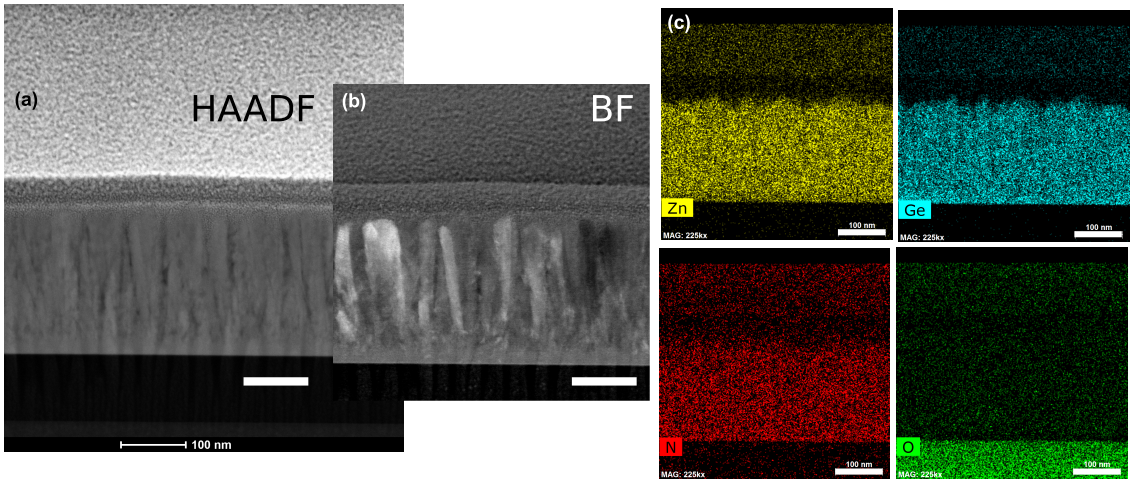


Fig. 5 TEM was collected for a 45% Zn/(Zn+Ge) sample synthesized at 300°C. All scale bars are 100 nm. (a) HAADF and (b) bright-field TEM show dense, columnar grains. (c) EDS maps indicate uniform distribution of Zn, Ge and N in the sample, and no O segregation is observed.

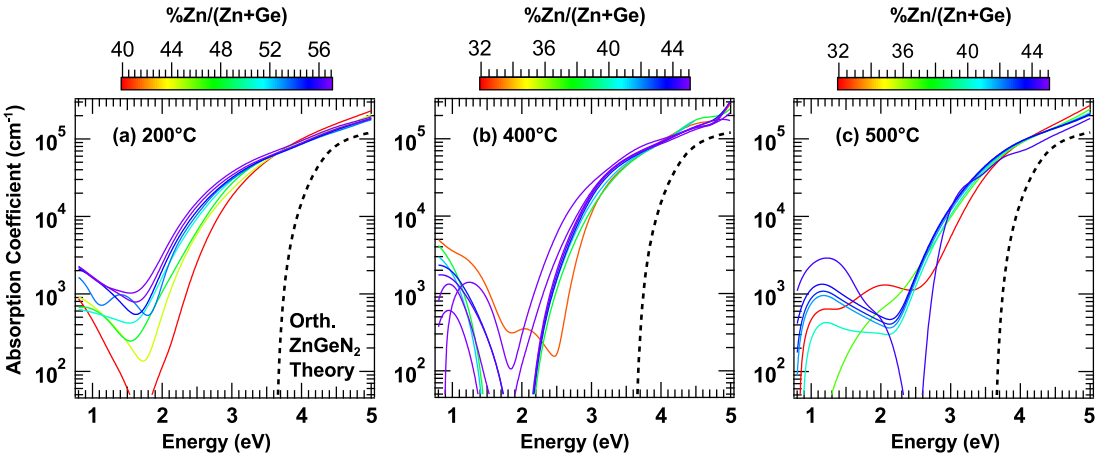


Fig. 6 Ellipsometry data was modelled to simulate the absorption coefficient as a function of energy for sample libraries grown at (a) 200°C, (b) 400°C and (c) 500°C, with cation composition shown on the color axes. Each library shows a different spread of cation compositions due to the change in incorporation of Zn as a function of temperature. The dashed trace is the theoretical absorption curve of cation-ordered $ZnGeN_2$.

combinatorial sputtered films.[35,37] The grains are fairly uniform in size but exhibit different crystallographic orientations, which is expected based on the XRD data. EDS shows that Zn, Ge, and N are distributed evenly throughout the sample, and no elemental segregation is observed. This validates the results found by Pawley refinement which suggest that excess cation off-stoichiometry is incorporated into the lattice by an alloy-like mechanism, instead of segregating at grain boundaries or amorphous inclusions. This sample was grown on a Si substrate with 100 nm of thermal oxide, which is why an O layer is present below the film.

### 3.4 Optical Properties

A selection of sample libraries was modelled using ellipsometry in order to extract optical constants and model absorption coefficient as a function of energy. Refractive index and extinction coefficient data for stoichiometric and Ge-rich samples is included in the Supplementary Information (Fig. S3). Fig. 6 shows this data for libraries synthesized at (a) 200°C, (b) 400°C and (c) 500°C. The color axis indicates cation composition of each sample; each library exhibits a different spread of cation compositions due to the change in Zn incorporation as a function of temperature. The absorption of these libraries acts as expected for a semiconductor: at low incident energies, the samples are fairly transparent (below $3\times10^3$ $cm^{-1}$), and at higher energies they begin absorbing and plateau at large absorption coefficients (approximately $10^5$ $cm^{-1}$). Some samples, especially Zn-rich samples, exhibit parasitic absorption below the absorption onset, implying defect states within the bandgap. All samples examined exhibit absorption onsets that are at least 1 eV below the calculated trace for orthorhombic (cation-ordered) $ZnGeN_2$ (shown as a dashed line). This shift is consistent with a decreased bandgap value with disorder on the cation site. Additionally, as Ge content increases, a continuous shift of the absorption onset to higher energies is observed (most easily observed in Fig. 6a).

To understand shifts with changing synthesis parameters, absorption data is plotted as a function of synthesis temperature

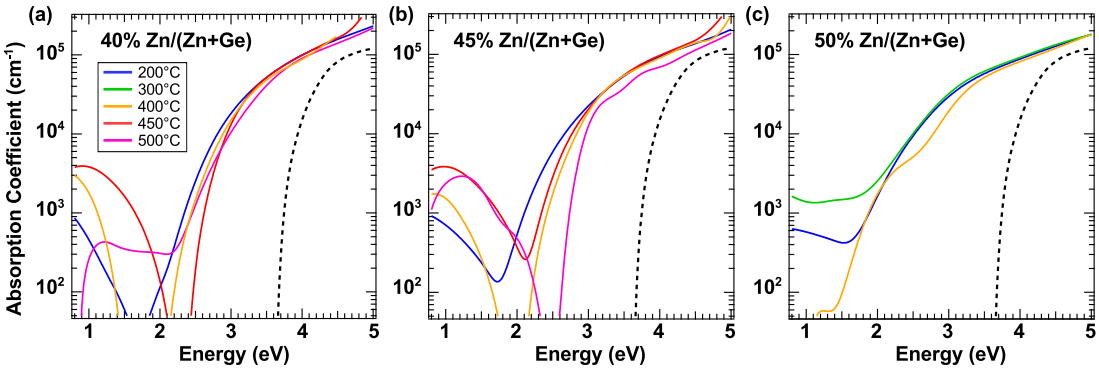


Fig. 7 Absorption curves at constant composition of (a) 40%, (b) 45% and (c) 50% Zn/(Zn+Ge). Increasing synthesis temperature tends to shift the absorption onset to higher energies. A general trend toward sharper absorption onset is seen with off-stoichiometry; the absorption onsets shown in (c) are much more gradual than those shown in (a).

at constant cation composition in Fig. 7. Since increasing synthesis temperature forces samples off-stoichiometric (Ge-rich) as discussed in Section 3.1, it is not possible to fully deconvolve the impacts of composition and temperature using this sample set; however, overarching trends can be observed. For both (a) 40% and (b) 45% Zn/(Zn+Ge), increasing temperature shifts the absorption to higher energies. This is consistent with the non-equilibrium energetics of sputtering, since a low-temperature synthesized film is expected to have a larger number of kinetically trapped defects than a higher-temperature film, which will be closer to equilibrium conditions. As shown in Fig. 7c, the absorption threshold at 50% Zn/(Zn+Ge) is ∼1 eV below the predicted band gap for orthorhombic (cation-ordered) $ZnGeN_2$. Though this curve is more gradual than the theoretical curve for ordered $ZnGeN_2$, indicating some amount of parasitic absorption due to absorbing defects, the absorption onset is definitively lower than predicted. This suggests that disorder on the cation site is reducing the absorption onset from the theoretical value at 50% Zn/(Zn+Ge). However, even synthesizing films slightly Ge-rich dramatically sharpens the absorption onset while still well below the cation-ordered theory (Fig. 7b), indicating high crystalline quality with fewer absorbing defects. This is consistent with the faceting observed by SEM only at off-stoichiometric compositions.

To quantify the shifts in absorption onset with changing stoichiometry, the energy value corresponding to an absorption coefficient of $10^4$ $cm^{-1}$ is plotted in Fig. 8 versus cation composition. This threshold value is here used as a proxy for optical bandgap, since it is straightforward to extract and less open-ended than the traditionally used Tauc fitting. It is important to note that the $10^4$ absorption threshold does not capture the complexity of a film's optical properties, and since these films do not exhibit photoluminescence it is challenging to make conclusions about the true optical bandgap from this data; however, it is useful to elucidate trends. The gray highlighted region indicates where the cell volume plateaus as a function of cation composition (same region as in Fig. 3c), indicating the non-alloy-like regime. The samples plotted in Fig. 8 were synthesized at different temperatures (demarcated by different color traces), and consequently have different composition ranges from Zn-rich (low temperature) to Ge-rich

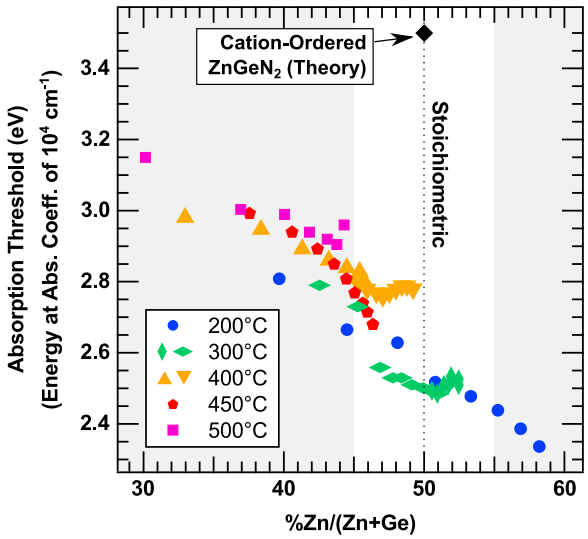


Fig. 8 The energy value at an absorption coefficient of $10^4$ $cm^{-1}$ can be used as a characteristic absorption threshold. Plotting this threshold as a function of cation composition reveals a continuous shift in absorption threshold with composition.

(high temperature).

The trend of increasing absorption threshold with increasing Ge content is observed for all libraries examined, with the highest energy absorption onset occurring at ∼30% Zn/(Zn+Ge) and the lowest occurring at 60%. This continuous trend is unexpected from a point defect perspective, since the simple cation antisite mechanism to explain off-stoichiometry would cause parasitic absorption to reduce the absorption onset both for Zn-rich and Ge-rich material. This is consistent with the Zn-rich results, but does not explain the increase in energy of the absorption onset for Ge-rich films. However, when we take into account the alloy-like cell volume shifts observed by Pawley refinement, the optical shift can be considered bandgap-bowing behavior. Thus, within the 45−55% Zn/(Zn+Ge) regime, changing cation composition is causing bandgap tuning similar to that of a traditional semiconductor alloy. As discussed in Section 3.2, the binary metal nitrides of Zn and Ge are not wurtzite, and thus bandgap charac-

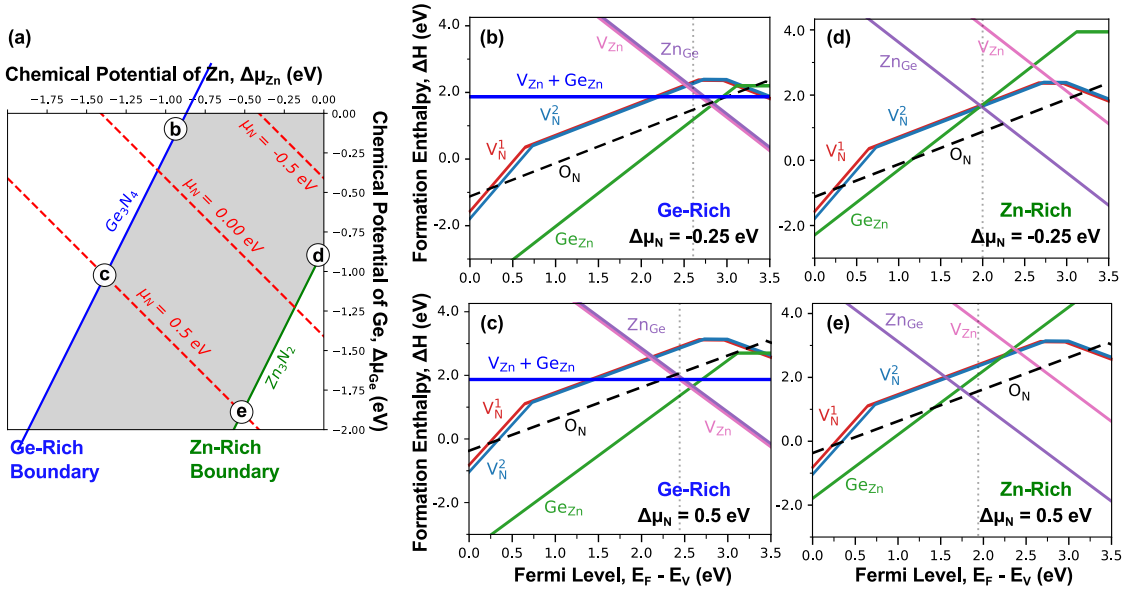


Fig. 9 (a) Chemical potential stability phase diagram for $ZnGeN_2$. (b-e) Defect formation energy plots corresponding to the respective points indicated in (a), which are in a Ge-rich regime (b-c) and a Zn-rich regime (d-e). The equilibrium Fermi levels are shown with vertical dashed gray lines.

teristics cannot be attributed to alloy composition-derived band bowing between $Zn_3N_2$ and $Ge_3N_4$; this behavior is instead enabled by cation disorder and the similar atomic sizes of Zn and Ge. Outside of the alloy-like regime the shifts to larger optical absorption remain unexplained. Regardless of mechanism, this result suggests that Ge-rich cation composition could be used to tune and sharpen the optical absorption of $ZnGeN_2$. Additionally, this result helps to frame the literature; reported bandgap values range from 2.7-3.4 eV, which could be explained by uncharacterized shifts in cation stoichiometry.[19–24]

### 3.5 Theoretical Energetics

In order to understand the stability of the $ZnGeN_2$ system with regard to off-stoichiometry, theoretical calculations were performed of native point defects as well as extrinsic oxygen. Fig. 9 shows the resulting defect diagrams that examine the formation enthalpy of different types of native and impurity point defects. Since sputtering explores different chemical potential regimes, defect diagrams were created for both Ge-rich and Zn-rich regimes where $ZnGeN_2$ is stable, and the nitrogen chemical potential was varied in order to simulate activated nitrogen. In sputtering, the nitrogen chemical potential can rise considerably above thermodynamic (negative) values.[54] We are considering $\Delta\mu_N = +0.5$ eV as a higher level of activation of the N source, and $\Delta\mu_N$ = -0.25 eV as a lower activation closer to the thermodynamical value. The limits of the Zn and Ge chemical potentials are determined by formation of $Zn_3N_2$ and $Ge_3N_4$, respectively, as shown in Fig. 9a. However, in a non-equilibrium situation, those boundaries may not be very well established and the effective $\Delta\mu_{Zn}$ and $\Delta\mu_{Ge}$ values could lie outside of those boundaries. Also, higher deposition temperatures should correspond to more Ge-rich regimes, due to the volatility of Zn.[55] The defects being considered are the native antisites ($Ge_{Zn}$ and $Zn_{Ge}$) as well as $O_N$ substitutional impurities, and vacancies of all three elements. The equilibrium Fermi levels (shown as vertical dashed lines) were calculated without the $O_N$ defect, since the samples reported here have minimal oxygen incorporation. In this defect model, most of the defects are calculated in the dilute condition and defect-defect interactions are only considered through pair binding energies, e.g. $V_{Zn}$ + $Ge_{Zn}$ pair. Since our films are highly disordered and can stabilize with cation off-stoichiometry, this is not a perfect model for our system; however, this model provides a framework with which to think about the mechanism behind off-stoichiometry and cation disorder.

Within the chemical potential region sampled within Fig. 9b-e, the equilibrium Fermi level naturally occurs either mid-gap or slightly toward the conduction band edge, indicating charge compensation rather than doping. This is consistent with the experimental observation that all films are insulating. A detailed inspection of Fig. 9b-e reveals that Zn and Ge antisites are always among the most favorable defects at the Fermi level, which agrees with the observed cation site disorder in the system and has been computationally predicted previously.[56,57] However, since mutually charge compensated anti-site defects do not accommodate off-stoichiometry, other defects must participate. The most likely pairs should be $V_{Zn}$+$Ge_{Zn}$ in the Ge-rich and $Zn_{Ge}$+$V_N$ in the Zn-rich regimes. This is observed in the Ge-rich regimes: the $Ge_{Zn}$ antisite is compensated by a Zn vacancy, and the defect complex between them is fairly low energy, which could all serve to drive off-stoichiometry. This agrees with the experimental phase map in Fig. 1: films can incorporate more off-stoichiometry when Ge-rich than Zn-rich. Overall, in all regimes these calculations suggest that the $ZnGeN_2$ system has a tendency for Zn and Ge site-swapping, which is also observed experimentally through both cation site disorder and off-stoichiometry.

One other conclusion that is evident from these calculations

is that changing the nitrogen chemical potential has an impact on the incorporation of oxygen in this structure, which is consistent with observed oxygen incorporation in our previous work (Ref. 35). With synthesis conditions where oxygen is present, $Zn_{Ge}+O_N$ pairs could also cause Zn rich compositions. Finally, these results indicate that sputtering is indeed enabling far off-equilibrium growth, since experimental defect concentrations (i.e. off-stoichiometry) are accessed that are far beyond the formation enthalpies in this defect model.

## 4 Conclusion

In this work, we have used combinatorial sputtering to explore the synthetic phase space of cation-disordered $ZnGeN_2$. We found that this compound crystallizes in the wurtzite structure at both Zn-rich and Ge-rich cation compositions, similar behavior to that observed in the related compound $ZnSnN_2$.[37] At Zn-rich compositions, films tend to exhibit preferential orientation in the (002) direction, which is consistent with previous findings and is a promising result for future epitaxial studies.[35] As synthesis temperature increases, films tend to grow Ge-rich due to Zn loss, which is consistent with theoretical defect diagrams. Since oxygen is only present at trace amounts in these films, this implies that the ability of this compound to stabilize at off-stoichiometric compositions is not linked to defect complex formation with oxygen, as predicted for $ZnSnN_2$.[39] Structural refinements of XRD data reveal a composition region from 45-55% Zn/(Zn+Ge) where cell volume shifts continuously with cation composition in an alloy-like manner, likely enabled by the close atomic sizes of Zn and Ge. Further theoretical and experimental work is necessary to investigate the local structure stabilizing $ZnGeN_2$ so far off-stoichiometry outside of this alloy-like regime.

Optical properties were characterized using spectroscopic ellipsometry and the optical absorption onset was found to be significantly below the value predicted for cation-ordered $ZnGeN_2$, suggesting that disorder is reducing the band gap as predicted. The absorption onset shifts to higher energies with increasing synthesis temperature for a given composition, but remains well below the value predicted for cation-ordered $ZnGeN_2$. Additionally, an increase in absorption onset with Ge-rich off-stoichiometry is observed, which may explain the spread in optical properties from the literature. This trend is consistent with an alloy-like model enabling bandgap tuning with cation off-stoichiometry, and could prove useful as an additional knob to tune optical properties. Additionally, the tolerance of the cation-disordered structure to off-stoichiometry raises the question of how this system will change when cation ordering is induced; it seems unlikely from an antisite perspective that off-stoichiometry and cation ordering can coexist, so can cation off-stoichiometry be used as a mechanism to trap site disorder in this system, as has been found in similar systems?[58] Understanding these interactions will require further investigation, but the use of cation composition as a tunable parameter offers new possibilities for optoelectronic development of $ZnGeN_2$.

## Conflicts of interest

There are no conflicts to declare.

## Acknowledgements

Primary funding was provided by the U.S. Department of Energy, Office of Science, Basic Energy Sciences, Materials Sciences and Engineering Division. This work was authored in part by the National Renewable Energy Laboratory, operated by Alliance for Sustainable Energy, LLC, for the U.S. Department of Energy (DOE) under Contract No. DE-AC36-08GO28308. Use of the SSRL, SLAC National Accelerator Laboratory, was supported by the DOE, SC, BES under Contract DE-AC02-76SF00515. We thank Dr. Suchismita Sarker and Dr. Apurva Mehta for assistance at SLAC BL1-5. This work was supported in part by the National Science Foundation Division of Materials Research under Grant No. 1555340 for diffraction analysis. R. R. S. acknowledges support from the National Science Foundation Graduate Research Fellowship under Grant No. 1646713 for ellipsometry measurements. A.M. acknowledges support of the CooksTek Fellowship in Advanced Ceramics at the Colorado School of Mines for transmission electron microscopy measurements.

## Notes and references

1 S. Nakamura, *Annalen der Physik*, 2015, **527**, 335–349.
2 *Oxide and nitride semiconductors: processing, properties, and applications*, ed. T. Yao and S.-K. Hong, Springer, Berlin, 2009, pp. 1–19.
3 M. Pattison, *2018 Solid-State Lighting R&D Opportunities*, Department of Energy technical report, 2019.
4 J. H. Park, D. Y. Kim, E. F. Schubert, J. Cho and J. K. Kim, *ACS Energy Letters*, 2018, **3**, 655–662.
5 H. Hu, S. Zhou, H. Wan, X. Liu, N. Li and H. Xu, *Scientific Reports*, 2019, **9**, 3447.
6 C. Goodman, *Journal of Physics and Chemistry of Solids*, 1958, **6**, 305–314.
7 R. Pamplin, *J. Phys. Chem. Solids*, 1963, **25**, 675–684.
8 A. D. Martinez, A. N. Fioretti, E. S. Toberer and A. C. Tamboli, *Journal of Materials Chemistry A*, 2017, **5**, 11418–11435.
9 S. Nakatsuka and Y. Nose, *The Journal of Physical Chemistry C*, 2017, **121**, 1040–1046.
10 W. L. Larson, H. P. Maruska and D. A. Stevenson, *Journal of The Electrochemical Society*, 1974, **121**, 1673–1674.
11 A. Punya, W. R. L. Lambrecht and M. van Schilfgaarde, *Phys. Rev. B*, 2011, **84**, 165204.
12 D. O. Scanlon and A. Walsh, *Applied Physics Letters*, 2012, **100**, 251911.
13 N. Feldberg, J. D. Aldous, W. M. Linhart, L. J. Phillips, K. Durose, P. A. Stampe, R. J. Kennedy, D. O. Scanlon, G. Vardar, R. L. Field, T. Y. Jen, R. S. Goldman, T. D. Veal and S. M. Durbin, *Applied Physics Letters*, 2013, **103**, 042109.
14 M. Maunaye and J. Lang, *Materials Research Bulletin*, 1970, **5**, 793–796.
15 E. W. Blanton, K. He, J. Shan and K. Kash, *Journal of Crystal Growth*, 2017, **461**, 38–45.
16 P. Narang, S. Chen, N. C. Coronel, S. Gul, J. Yano, L. W. Wang, N. S. Lewis and H. A. Atwater, *Advanced Materials*, 2014, **26**, 1235–1241.

17 S. Kikkawa and H. Morisaka, *Solid State Communications*, 1999, **112**, 513–515.

18 Q. H. Zhang, J. Wang, C. W. Yeh, W. C. Ke, R. S. Liu, J. K. Tang, M. B. Xie, H. B. Liang and Q. Su, *Acta Materialia*, 2010, **58**, 6728–6735.

19 T. Misaki, A. Wakahara, H. Okada and A. Yoshida, *Journal of Crystal Growth*, 2004, **260**, 125–129.

20 L. Zhu, P. Maruska, P. Norris, P. Yip and L. Bouthillette, *MRS Proceedings*, 1998, **537**, 291–296.

21 K. Du, C. Bekele, C. C. Hayman, J. C. Angus, P. Pirouz and K. Kash, *Journal of Crystal Growth*, 2008, **310**, 1057–1061.

22 T. Misaki, K. Tsuchiya, D. Sakai, A. Wakahara, H. Okada and A. Yoshida, *Physica Status Solidi (c)*, 2003, **0**, 188–191.

23 R. Viennois, T. Taliercio, V. Potin, A. Errebbahi, B. Gil, S. Charar, A. Haidoux and J.-C. Tédenac, *Materials Science and Engineering: B*, 2001, **82**, 45–49.

24 L. Zhu, P. Norris and L. Bouthillette, *MRS Proceedings*, 1999, **607**, 291–291.

25 M. B. Tellekamp, C. L. Melamed, A. G. Norman and A. Tamboli, *Crystal Growth & Design*, 2020, **20**, 1868–1875.

26 M. R. Karim, B. H. D. Jayatunga, Z. Feng, K. Kash and H. Zhao, *Crystal Growth & Design*, 2019, **19**, 4661–4666.

27 S. Lany, A. N. Fioretti, P. P. Zawadzki, L. T. Schelhas, E. S. Toberer, A. Zakutayev and A. C. Tamboli, *Phys. Rev. Materials*, 2017, **1**, 035401.

28 R. Schnepf, J. J. Cordell, M. B. Tellekamp, C. L. Melamed, A. L. Greenaway, A. Mis, G. L. Brennecka, S. T. Christensen, G. J. Tucker, E. S. Toberer, S. Lany and A. Tamboli, *ACS Energy Letters*, 2020, **Just Accepted Manuscript**,.

29 J. Breternitz, Z. Wang, A. Glibo, A. Franz, M. Tovar, S. Berendts, M. Lerch and S. Schorr, *physica status solidi (a)*, 2019, 1800885.

30 N. Zhang, S. Ouyang, T. Kako and J. Ye, *Chem. Commun.*, 2012, **48**, 1269–1271.

31 X. Wang, K. Maeda, Y. Lee and K. Domen, *Chemical Physics Letters*, 2008, **457**, 134–136.

32 F. Tessier, P. Maillard, Y. Lee, C. Bleugat and K. Domen, *The Journal of Physical Chemistry C*, 2009, **113**, 8526–8531.

33 Y. Lee, K. Teramura, M. Hara and K. Domen, *Chemistry of Materials*, 2007, **19**, 2120–2127.

34 P. Bacher, G. Roult, M. Ghers, O. Merdrignac, J. Guyader and Y. Laurent, *Materials Chemistry and Physics*, 1989, **21**, 223–235.

35 C. L. Melamed, M. B. Tellekamp, J. S. Mangum, J. D. Perkins, P. Dippo, E. S. Toberer and A. C. Tamboli, *Physical Review Materials*, 2019, **3**, 051602.

36 E. Arca, A. Fioretti, S. Lany, A. C. Tamboli, G. Teeter, C. Melamed, J. Pan, K. N. Wood, E. Toberer and A. Zakutayev, *IEEE Journal of Photovoltaics*, 2018, **8**, 110–117.

37 A. N. Fioretti, A. Zakutayev, H. Moutinho, C. Melamed, J. D. Perkins, A. G. Norman, M. Al-Jassim, E. S. Toberer and A. C. Tamboli, *J. Mater. Chem. C*, 2015, **3**, 11017–11028.

38 A. N. Fioretti, A. Stokes, M. R. Young, B. Gorman, E. S. Toberer, A. C. Tamboli and A. Zakutayev, *Advanced Electronic Materials*, 2017, **3**, 1600544.

39 A. N. Fioretti, J. Pan, B. R. Ortiz, C. Melamed, P. C. Dippo, L. T. Schelhas, J. D. Perkins, D. Kuciauskas, S. Lany, A. Zakutayev, E. S. Toberer and A. C. Tamboli, *Materials Horizons*, 2018, **5**, 823–830.

40 E. Arca, S. Lany, J. D. Perkins, C. Bartel, J. Mangum, W. Sun, A. Holder, G. Ceder, B. Gorman, G. Teeter, W. Tumas and A. Zakutayev, *Journal of the American Chemical Society*, 2018, **140**, 4293–4301.

41 K. R. Talley, S. R. Bauers, C. L. Melamed, M. C. Papac, K. N. Heinselman, I. Khan, D. M. Roberts, V. Jacobson, A. Mis, G. L. Brennecka, J. D. Perkins and A. Zakutayev, *ACS Combinatorial Science*, 2019, **21**, 537–547.

42 A. D. Martinez, E. M. Miller, A. G. Norman, R. R. Schnepf, N. Leick, C. Perkins, P. Stradins, E. S. Toberer and A. C. Tamboli, *Journal of Materials Chemistry C*, 2018, **6**, 2696–2703.

43 N. Barradas, K. Arstila, G. Battistig, M. Bianconi, N. Dytlewski, C. Jeynes, E. Kótai, G. Lulli, M. Mayer, E. Rauhala, E. Szilágyi and M. Thompson, *Nuclear Instruments and Methods in Physics Research Section B: Beam Interactions with Materials and Atoms*, 2008, **266**, 1338–1342.

44 L. Giannuzzi and F. Stevie, *Micron*, 1999, **30**, 197–204.

45 G. Kresse and D. Joubert, *Physical Review B*, 1999, **59**, 1758.

46 J. P. Perdew, K. Burke and M. Ernzerhof, *Physical Review Letters*, 1996, **77**, 3865.

47 S. Dudarev, G. Botton, S. Savrasov, C. Humphreys and A. Sutton, *Physical Review B*, 1998, **57**, 1505.

48 J. Pan, J. Cordell, G. J. Tucker, A. C. Tamboli, A. Zakutayev and S. Lany, *Advanced Materials*, 2019, **31**, 1807406.

49 L. Y. Lim, S. Lany, Y. J. Chang, E. Rotenberg, A. Zunger and M. F. Toney, *Phys. Rev. B*, 2012, **86**, 235113.

50 S. Lany, *Phys. Rev. B*, 2013, **87**, 085112.

51 D. Partin, D. Williams and M. O'Keeffe, *Journal of Solid State Chemistry*, 1997, **132**, 56–59.

52 B. Molina and L. E. Sansores, *International Journal of Quantum Chemistry*, 2000, **80**, 249–257.

53 J. A. Thornton, *Annual Review of Materials Science*, 1977, **7**, 239–260.

54 C. M. Caskey, R. M. Richards, D. S. Ginley and A. Zakutayev, *Mater. Horiz.*, 2014, **1**, 424–430.

55 C. B. Alcock, V. P. Itkin and M. K. Horrigan, *Canadian Metallurgical Quarterly*, 1984, **23**, 309–313.

56 D. Skachkov, A. Punya Jaroenjittichai, L.-y. Huang and W. R. L. Lambrecht, *Physical Review B*, 2016, **93**, 155202.

57 D. Skachkov, P. C. Quayle, K. Kash and W. R. L. Lambrecht, *Phys. Rev. B*, 2016, **94**, 205201.

58 R. R. Schnepf, B. L. Levy-Wendt, M. B. Tellekamp, B. R. Ortiz, C. L. Melamed, L. T. Schelhas, K. H. Stone, M. F. Toney, E. S. Toberer and A. C. Tamboli, *Journal of Materials Chemistry C*, 2020, **8**, 4350–4356.

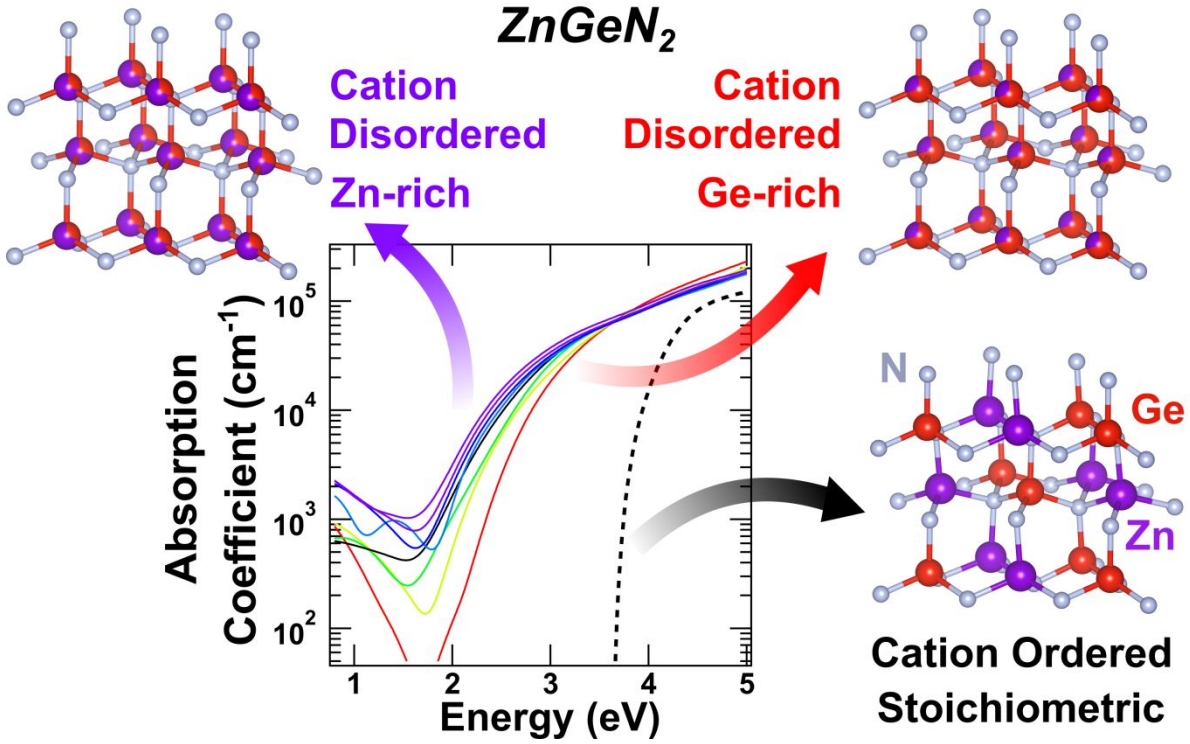


Cation-disordered $ZnGeN_2$ is found to exhibit structural and optical tunability with cation off-stoichiometry.